Micro-Raman spectroscopy of mechanically exfoliated few-quintuple layers of Bi_2Te_3, Bi_2Se_3, and Sb_2Te_3 materials

K. M. F. Shahil,[a)] M. Z. Hossain,[b)] V. Goyal,[c)] and A. A. Balandin[d)]

Department of Electrical Engineering, Materials Science and Engineering Program,
Bourns College of Engineering, University of California - Riverside, Riverside, California 92521, USA

Bismuth telluride (Bi_2Te_3) and related compounds have recently attracted strong interest, owing to the discovery of the topological insulator properties in many members of this family of materials. The few-quintuple films of these materials are particularly interesting from the physics point of view. We report results of the micro-Raman spectroscopy study of the "graphene-like" exfoliated few-quintuple layers of Bi_2Te_3, Bi_2Se_3, and Sb_2Te_3. It is found that crystal symmetry breaking in few-quintuple films results in appearance of A_{1u}-symmetry Raman peaks, which are not active in the bulk crystals. The scattering spectra measured under the 633-nm wavelength excitation reveals a number of resonant features, which could be used for analysis of the electronic and phonon processes in these materials. In order to elucidate the influence of substrates on the few-quintuple-thick topological insulators, we examined the Raman spectra of these films placed on mica, sapphire, and hafnium-oxide substrates. The obtained results help to understand the physical mechanisms of Raman scattering in the few-quintuple-thick films and can be used for nanometrology of topological insulator films on various substrates. © *2012 American Institute of Physics*. [http://dx.doi.org/10.1063/1.3690913]

I. INTRODUCTION

Topological insulators (TI) constitute a new class of materials, which recently attracted significant attention of the physics and device research communities. The TI materials were shown to have an unusual insulating gap and exhibit quantum-Hall-like behavior in the absence of a magnetic field.[1–8] The strong spin-orbit coupling dictates robust surface states, which are topologically protected against back scattering from time-reversal invariant defects and impurities. It was suggested that TIs can be used for fault-tolerant quantum computing.[7,8] The unique properties of TIs show promise for the dissipation-less quantum electronics and spintronic devices operating at room temperature (RT). The thin films made of TI materials were proposed for applications in magnetic memory, where write and read operations can be achieved by purely electric means.[8]

It has been experimentally demonstrated that the bismuth telluride (Bi_2Te_3) family of materials, e.g., Bi_2Te_3, Bi_2Se_3 and Sb_2Te_3, are TIs with energy gaps and gapless surface states consisting of a Dirac cone.[4–6] In addition to their new role as TIs, Bi_2Te_3 and related materials are among the best and widely used thermoelectric materials for near RT applications.[9–13] Apart from being thermoelectric materials, Bi_2Se_3 was also used in infrared detectors,[14] while Sb_2Te_3 was utilized in chalcogenide alloys as the phase changing material for information storage.[15]

Despite increasing interest to Bi_2Te_3, Bi_2Se_3, and Sb_2Te_3 as TIs and their significance for thermoelectric industry, very few Raman spectroscopy studies of these materials were reported to date.[16–22] Most of the published Raman studies of these materials investigate bulk crystals or relatively thick film ($\sim\mu$m range), which are either amorphous or polycrystalline. The Raman spectroscopy data can provide useful structural information, crystalline phase, composition, and stoichiometry of the samples. It helps in understanding phonon dynamics and optical properties as well as serves as the means for determining the strain and compression in thin films and nanostructures. Most recently, micro-Raman spectroscopy became valuable as a nanometrology tool for graphene. It allows one to count, accurately and non-destructively, the number of atomic planes in graphene samples,[23] determine its quality, and identify graphene on variable substrates and at different temperatures.[24] Raman spectroscopy was also used for the very first measurement of thermal conductivity of graphene.[25]

Here, we report a systematic micro-Raman spectroscopy study of the thin crystalline films of Bi_2Te_3, Bi_2Se_3, and Sb_2Te_3. The samples for this study were prepared via the "graphene-like" mechanical exfoliation. We have recently successfully applied this technique for fabrication of the atomically thin single-crystal films and ribbons of Bi_2Te_3[26] and investigation of their electrical and electronic noise properties.[27] The developed exfoliation technique can be readily extended to other thermoelectric material systems.[28] The single-crystal Bi_2Te_3, Bi_2Se_3, and Sb_2Te_3 films with the thicknesses of just a few nanometers were prepared via the "graphene-like" exfoliation process. The resulting few-quintuple layer (FQL) films are well suited for both investigation of their physical properties and potential device applications.

[a)]Present address: Intel Corporation, Hillsboro, Oregon 97124, USA.
[b)]Present address: Micron Technology, Boise, Idaho 83707, USA.
[c)]Present address: Texas Instruments, Dallas, Texas 75243, USA.
[d)]Author to whom correspondence should be addressed. Electronic mail: balandin@ee.ucr.edu. URL: http://ndl.ee.ucr.edu.

In the present research, we focused on FQL structures. Owing to the low thermal conductivity of Bi_2Te_3 and related materials, a systematic Raman study of individual quintuples is complicated by a strong local heating and melting, even at low laser excitation power. It has also been suggested that FQL are more promising as TI structures. While the bandgap in a single quintuple is larger than in FQL, the latter has less coupling between the surface states of the top and bottom interfaces. The FQL Bi_2Te_3, Bi_2Se_3, and Sb_2Te_3 films are also more practical for thermoelectric applications. Taking the graphene[29] analogy even further, we propose micro-Raman spectroscopy as a nanometrology tool for identification of FQL films of topological insulators and for assessing their quality.[30] Extending our previous investigation, in this paper, we present a systematic study of the thin films made of several materials—Bi_2Te_3, Bi_2Se_3, and Sb_2Te_3—which constitute some of the most promising TI and thermoelectric systems.

II. CRYSTAL STRUCTURE AND LATTICE VIBRATIONS

The B_V-A_{VI} compounds (i.e., Bi_2Te_3, Bi_2Se_3, and Sb_2Te_3) exhibit a layered, rhombohedral, crystal structure of the space group $R\bar{3}m(D_{3d}^5)$.[16–19] These materials are built of anisotropic layers, in which five atomic planes are covalently bonded to form a *quintuple* layer, as shown in Fig. 1(a). A *quintuple* consists of five mono-atomic planes of $A_{VI}^{(1)}$-B_V-$A_{VI}^{(2)}$-B_V-$A_{VI}^{(1)}$. Here, A_{VI} can be either Te or Se and B_V either Bi or Sb. The superscripts on the A_{VI} atoms designate the different positions within the fivefold layer. The 5-layer stacks are centro-symmetrical with respect to $A_{VI}^{(2)}$, which plays a role of an inversion center.[18] The conventional unit cell spans over three quintuple layers, and each quintuple layer has a thickness of $H \sim 1$ nm (see Fig. 1(a)). The quintuple layers are weakly bound to each other by the van der Waals forces that allow one to disassemble a B_V-A_{VI} crystal into its building blocks. In some cases, the atomic five-folds can be broken further into sub-quintuple, leading to B_V-A_{VI} atomic bi-layers and B_V-A_{VI}-B_V atomic tri-layers. While the bandgap in a single quintuple is larger than in FQL, the latter has less coupling between the surface states of the top and bottom interfaces.

The normal modes of vibration propagating along trigonal C_H axis involve motions of the entire planes of atoms, either parallel or perpendicular to C_H, and thus depend directly upon the inter-planar forces. At the Brillouin zone center, there are four distinct representations, namely, $2\Gamma_1^+$, $2\Gamma_3^+$, $3\Gamma_2^-$, and $3\Gamma_3^-$.[19] These phonon modes are exclusively either Raman or infrared (IR) active, due to the inversion crystal symmetry.[18] The Γ_1^+ and Γ_3^+ modes are Raman active, while the Γ_2^- and Γ_3^- modes of non-zero frequency are infrared active. So bulk crystals reveal 15 lattice vibration modes (phonon polarization branches). Three of these branches are acoustic and 12 are optical phonons. According to the group theory classification, 12 optical branches have $2A_{1g}$, $2E_g$, $2A_{1u}$, and $2E_u$ symmetry.[18] The corresponding Raman tensors of the Raman active modes are as follows:[18]

$$E_g = \begin{pmatrix} 0 & -c & -d \\ -c & 0 & 0 \\ -d & 0 & b \end{pmatrix} \quad \text{or} \quad \begin{pmatrix} c & 0 & 0 \\ 0 & -c & d \\ 0 & d & 0 \end{pmatrix},$$
$$A_{1g} = \begin{pmatrix} a & 0 & 0 \\ 0 & a & 0 \\ 0 & 0 & b \end{pmatrix}. \tag{1}$$

Here, the letters "E" and "A" indicate the in-plane and out-of-plane (C_H axis) lattice vibrations, respectively. The subscript "g" denotes Raman-active, while "u" stands for IR-active modes. The optical modes belonging to A_{1u} and E_u are allowed to be infrared active.

According to the selection rule given in Eq. (1), the off-diagonal Raman tensor components of the E_g mode distinguish themselves from A_{1g} mode. This is because a phonon of this type possesses displacements in both x- and y-direction. In the E_g^1 and A_{1g}^1, modes, the outer B_V-$A_{VI}^{(1)}$ pairs move in phase. Thus, the B_V-$A_{VI}^{(2)}$ bonding forces will be primarily involved in these vibrations; whereas, in the E_g^2 and A_{1g}^2 modes, the outer B_V and $A_{VI}^{(1)}$ atoms move in the opposite phase and are mainly affected by the forces between B_V and $A_{VI}^{(1)}$ atoms. The nearest-neighbor distances between B_V and A_{VI}^1 atoms are smaller than those between B_V and $A_{VI}^{(2)}$ atoms.[18] For this reason, the A_{1g}^1 and E_g^1 modes occur at lower frequencies than the A_{1g}^2 and E_g^2 modes.

III. EXPERIMENTAL DETAILS

A. Sample preparation

The FQL samples of Bi_2Te_3 and related materials (Bi_2Se_3, Sb_2Te_3) were separated from the bulk samples using a micro-mechanical cleavage process similar to that used for exfoliation of single layer graphene.[29] The "graphene-like" mechanical exfoliation from bulk crystals allowed us to obtain the high-quality crystalline films, which were important for this study. The exfoliated films were examined using a combination of the optical microscopy, atomic force microscopy (AFM), and scanning electron microscopy (SEM) to obtain thickness of a few atomic planes. All FQL layers were exfoliated on Si/SiO₂ substrate. An optical image of the exfoliated Bi_2Te_3 FQL is shown in Fig. 1(b). The detailed sample preparation and identification techniques were described by some of us elsewhere.[26,27,30]

All exfoliated FQL films were investigated with the high-resolution field emission scanning electron microscope (SEM, XL-30 FEG) operated at 10-15 kV. Representative high-resolution SEM micrographs in Figs. 1(c)–1(f) show SEM images of the reference bulk Bi_2Te_3 samples and FQL films of Sb_2Te_3, Bi_2Se_3, and Bi_2Te_3, respectively. All FQL films have the lateral sizes ranging from a few microns to tens of microns. Some FQL samples show a uniform surface and have correct geometrical shapes indicative of the facets and suggesting the high degree of crystallinity. The selected area electron diffraction of the crystalline structures of the layers was studied using FEI-PHILIPS CM300 transmission electron microscopy (TEM). The sample preparation for TEM inspection was carried out through ultrasonic
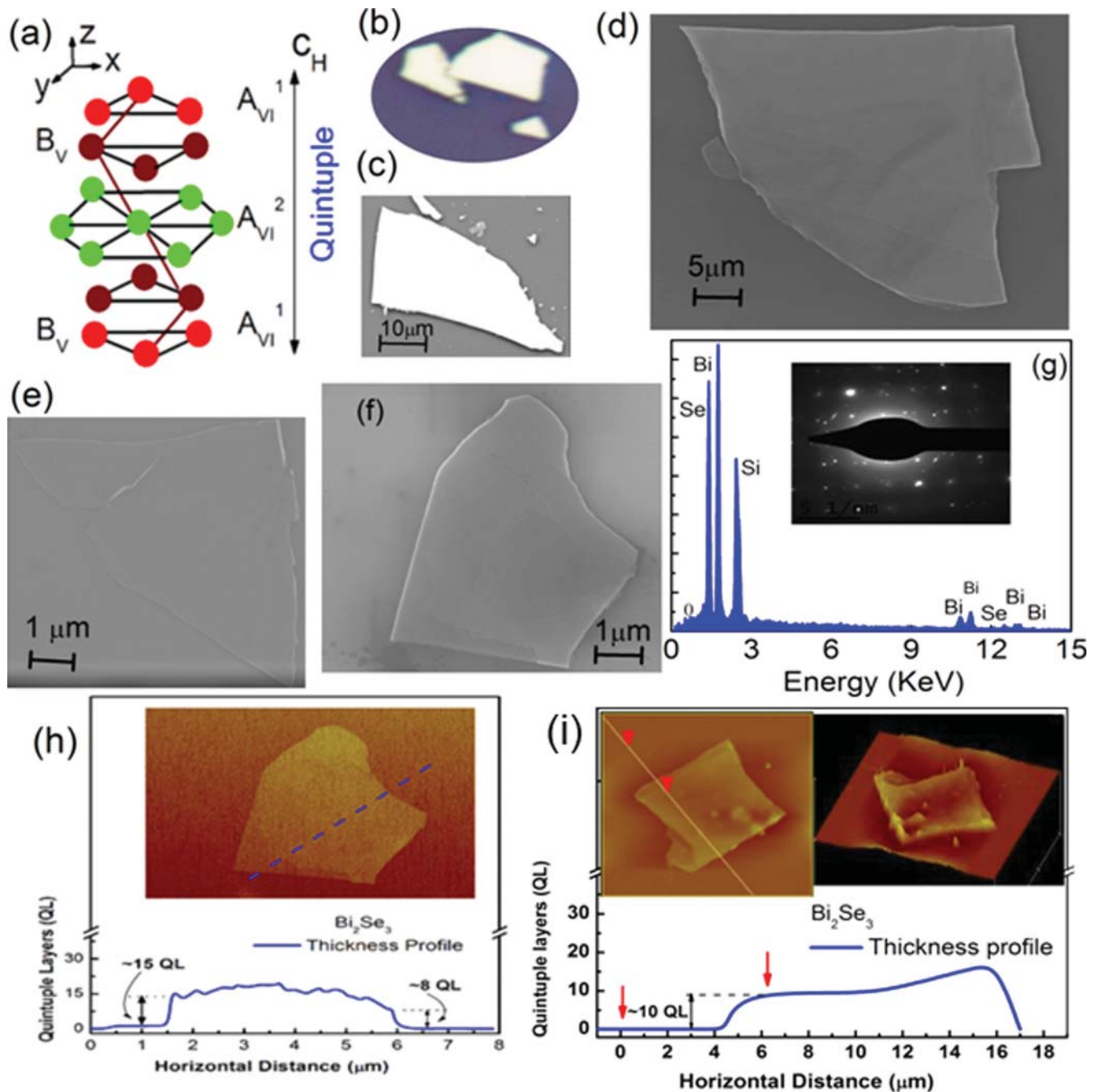
FIG. 1. (Color online) (a) Crystal structure of the B_V-A_{VI} compounds and a quintuple layer with the A_{VI}^2 (Te^2, Se^2) atoms as the inversion centers. (b) Optical image of exfoliated FQL of Bi_2Te_3. SEM images of (c) bulk Bi_2Te_3 and (d)-(f) exfoliated B_V-A_{VI} FQL, with the large lateral dimensions showing Sb_2Te_3, Bi_2Se_3, and Bi_2Te_3 flakes, respectively. (g) Structural and compositional characterization data showing EDS spectrum and electron diffraction pattern of Bi_2Se_3 FQL (inset), indicating the crystalline nature of the film. (h),(i) AFM images of FQL of Bi_2Se_3.

separation of dissolved samples in isopropyl alcohol (IPA). The samples were then transferred onto carbon-coated copper grids and studied under electron beam energy of 300 kV. The inset to Fig. 1(g) shows a representative electron diffraction pattern of Bi_2Se_3, which indicates the Bi-Se sample's perfect crystalline nature.

It is known that Bi_2Te_3 can be made either *n* or *p* type by changing the Bi/Te ratio. Even though the material that we use is pure Bi_2Te_3, the Bi/Te composition can deviate from the stoichiometric due to Bi/Te differential surface tension effects and constitutional supercooling effects. The composi-

tion control is a serious technical problem, because the thermoelectric properties of Bi_2Te_3 strongly depend on the composition. The defect chemistry in Bi_2Se_3 is dominated by the charged selenium vacancies, which act as the electron donors, resulting in *n*-type behavior. In this work, the elemental composition of FQL Bi-Se films was studied by the energy dispersive spectrometry (EDS) using Philips XL-30 FEG field-emission system. The molar contents of Bi and Se were found to be ∼38.98% and 54.55%, respectively. Figure 1(g) presents the EDS spectrum of Bi_2Se_3 FQL. A pronounced peak of Si indicates the electron beam penetration through

thin FQL Bi_2Se_3 films. The diffraction patterns (Fig. 1(g) inset) of the crystalline structures of the layers were studied using transmission electron microscopy (TEM).

The AFM studies were performed using a VEECO instrument with the vertical resolution down to ~0.1 nm in order to estimate the thickness of FQLs. The thickness of the atomic quintuple is H ~ 1 nm, which can be clearly distinguished with AFM by the step-like changes in the cleaved layers. The high-resolution AFM images of the exfoliated Bi_2Se_3 FQL are shown in Figs. 1(h)–1(i). The thickness of the films was measured along the line scan (see insets to the figures). The thickness profile is re-plotted (Fig. 1(h)), showing an 8-nm (~8 quintuple) step with respect to the substrate. In Fig. 1(i), another AFM image of Bi_2Se_3 is presented with the height profile and more uniform surface.

B. Raman instrumentation

An upgraded Renishaw inVia micro-Raman spectrometer RM 2000 was used for this study. All spectra were excited at room temperature with laser light $\lambda = 488$ nm and $\lambda = 633$ nm recorded in the backscattering configuration through a $50\times$ objective. With the 1800 lines/mm grating at 488 nm excitation and picking off the high resolution (-1 order), we can have the "hardware" spectral resolution of $1.35\,cm^{-1}$ (~$1\,cm^{-1}$). It was software-enhanced to $0.5\,cm^{-1}$, so that we were able to see the difference between peaks (with plotted Lorentzians) down to approximately ~$0.5\,cm^{-1}$. At the 633 nm excitation, the corresponding value of the spectral resolution was $0.63\,cm^{-1}$.

The Raman spectroscopic studies of thin films made from these materials are complicated, due to the local heating effects, since the materials have very low thermal conductivity and melting temperature.[26] The maximum excitation power of the Ar+ laser with the wavelength of 488 nm used in this study was 10 mW. Approximately half of the excitation power reaches the sample surface after transmission through the optical system. The local laser-induced heating results in local melting or oxidation of FQL films.[26,30] On the other hand, the measurement taken at insufficient excitation power produces low signal-to-noise (S/N) ratio, since the Raman spectra of these low-bandgap materials generally show the lower Raman count, owing to their metallic behavior. From the trial-and-error studies, we established that the optimum excitation power in our setup was ~0.2 mW on the sample surface. It provided a good signal-to-noise (S/N) ratio without damaging the FQL samples.

IV. RESULTS AND DISCUSSION

A. Non-resonant Raman spectra

The measured non-resonant Raman spectra of Bi_2Te_3 FQLs are shown in Fig. 2. The spectra are recorded under 488 nm excitation. The observed four optical phonon peaks are identified (see Table I). The frequencies of all these four zone-center regular Raman active modes are E_g^1 (TO) ~1.02 THz, A_{1g}^1 (LO) ~1.81 THz, E_g^2 (TO) ~3.02 THz, and A_{1g}^2 (LO) ~4 THz.[19] These peaks are very close to the previously measured and assigned Raman peaks of the Bi_2Te_3 bulk sample.[18–21] In
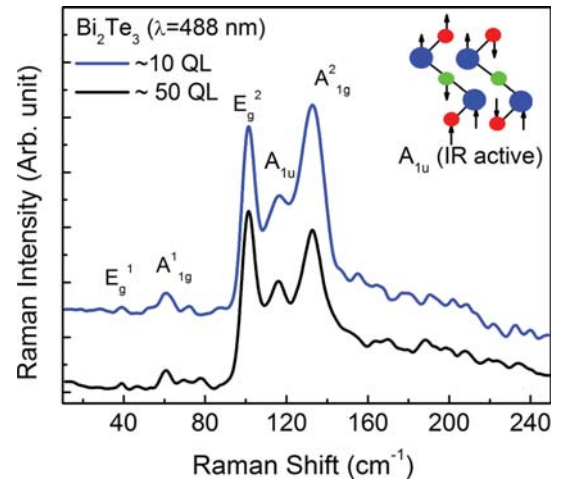

FIG. 2. (Color online) Raman spectrums of Bi_2Te_3 FQLs on Si/SiO_2 substrate. Spectra are taken from the spots with different thicknesses (~10 nm and ~50 nm) to demonstrate reproducibility. The displacement patterns of A_{1u} phonon mode are shown in inset.

addition to these peaks, another peak, $A_{1u} = 116.7\,cm^{-1}$ is found for the atomically thin FQL Bi_2Te_3 films. The A_{1u} mode of the longitudinal optical (LO) phonons at $116.7\,cm^{-1}$ is IR active and corresponds to the zone-boundary phonon (Z point) of the frequency ~3.57 THz.[18,19] According to the theory,[31] in crystals with the inversion symmetry, the IR-active modes, like A_{1u}, must be odd parity, while the Raman-active modes E_g, A_{1g} must be even parity under inversion. The phonon displacement vector Q of an odd-parity phonon (IR) changes the sign under inversion; hence the Raman tensor $(d\chi/dQ)$ of the odd-parity phonons in the centrosymmetric crystals must vanish[31] (see Eq. (1)). Thus, the odd-parity phonons (A_{1u}, E_u) do not show up in Raman spectra of bulk samples[20,21] as long as the crystal retains its symmetry. We attribute the appearance of A_{1u} mode in FQL to breaking of the crystal symmetry in the third dimension due to the limited thickness of FQL and presence of the interfaces.

We estimated the light penetration depth in our samples to be ~60–90 nm for a 488 nm laser, depending on the carrier concentration. One can calculate the penetration depth from the equation $\delta = 1/\sqrt{\pi f \sigma \mu}$, where f is the frequency of light, σ is the electrical conductivity of the materials, and μ is the magnetic permeability. We assumed σ in the range from 1.1×10^5 S/m to 5×10^4 S/m (Ref. 26), and then calculated the penetration depth to be from ~60 nm to 90 nm at 488 nm laser light. This value correlates well with thickness H when the $117\,cm^{-1}$ peak appears in FQL's spectrum. The onset of the A_{1u} peak at the moment when the penetration depth becomes equal to that of the FQL thickness suggests

TABLE I. Raman peaks in FQL Bi_2Te_3 films.

	E_g^1	A_{1g}^1	E_g^2	A_{1u}	A_{1g}^2	Comments
10 nm	38.5	60.7	101.4	116.5	132.9	This work
50 nm	39	61.1	101.5	116	132.39	
Bulk	36.5	62.0	102.3	…	134.0	Ref. 17
Bulk	…	62.3	103.7	…	134.2	Ref. 21

that the loss of the translation symmetry at the FQL–-substrate interface is the main mechanism of the crystal symmetry breaking.

Our results are in agreement with a recent computational study,[32] which found that the crystal symmetry breaking in Bi_2Te_3 thin films should lead the Raman activity of A_{1u}. The *ab initio* calculation, which included the spin-orbit (SO) coupling, found that the single quintuple-layer films and the bulk materials have different symmetries.[32] The film has P-3m[1] symmetry, while the bulk has R-3 m symmetry. It was also noted that, because of their limited thickness, the films have no translational symmetry in the third dimension. The loss of the translational symmetry in films was considered to be one of the crystal breaking mechanisms. Another possible mechanism for very thin films identified in Ref. 32 was a strong inharmonic potential that exists around Bi atoms in the single quintuple films, which can be one of the symmetry breaking mechanisms caused by SO interactions. We also note that a single quintuple is inversely symmetric. Breaking of the individual quintuple layers to sub-quintuples, which, in principle, is possible, particularly on the film surface, could be an extra mechanism leading the crystal symmetry breaking and appearance of the A_{1u} peak. The effect from such sub-quintuple breaking will become stronger as the thickness of the films and, correspondingly, the Raman interaction volume decreases.

As evidenced from ARPES measurements, an energy gap exists below a thickness of six quintuple layers of Bi_2Se_3 (Ref. 33) and the films preserve gapless surface states when the thickness is above six QL. On the other hand, a significant improvement in thermoelectric applications could be achieved in a 2D structure, where electrons and holes are strongly confined in one or two dimensions. With this in mind, we calibrated the intensity ratio of highest-frequency A_{1g} (i.e., A_{1g}^2 ∼4 THz) mode to that of Eg^2 mode (Eg^2 is the most pronounced feature in the spectrum), shown in Fig. 3. We found that the intensity ratio grows as the thickness decreases from the bulk to a few quintuple layers. It is reasonable to assume that the out-of-plane vibrations will be less restrained in a four-quintuple film than in bulk, which may lead to larger
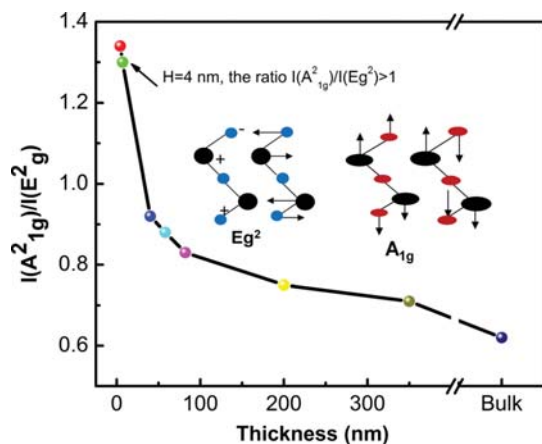
amplitudes of vibrations. According to a theoretical calculation,[32] there is another infra-active mode, A_{2u}, around ∼3.97 Thz. This peak may also become Raman active due to the symmetry breaking. However, it is difficult to distinguish these two peaks experimentally, because they are too close to each other. The strength of the Raman intensity of A_{1g}^2 mode (∼4 THz) can increase due to the activation of another IR mode, which is close to the A_{1g}^2 mode frequency. In this case, a combination of two Raman-active ($A_{1g}^2 + A_{2u}$) modes, with an average frequency of ∼4.03 THz, will appear as the Raman signature around ∼132 cm^{-1} with increased intensity. The discussed modifications of the characteristic peaks in Raman spectra of FQL Bi_2Te_3 with the thickness create a basis for the use of micro-Raman spectroscopy as a nanometrology tool for characterization of these unique structures with the potential for practical applications.

We now turn to the analysis of Raman spectrum of FQL Bi_2Se_3 films. Figure 4 shows Raman spectra of Bi_2Se_3 FQLs taken in the geometry $z(xx)\bar{z}$, i.e., incident light shines along the z direction and both the incident and scattered light are polarized along the x direction. There are three characteristic peaks within the scanned frequency range: ∼71 cm^{-1}, ∼131 cm^{-1}, and ∼173 cm^{-1}, which are identified in Raman spectra. From the Raman selection rules given in Ref. 18, it follows that the peak at 131.5 cm^{-1} has to be assigned to the E_g^2 mode, whereas the other two (71 cm^{-1} and 171.5 cm^{-1}) corresponds to A_{1g} mode. The observed frequencies are well comparable with the previously reported experimental and calculated phonon vibration modes of Bi_2Se_3 (Ref. 18) (see Table II). If polarization of the x direction is present ($z(xx)\bar{z}$ geometry), one will observe phonons denoted by A_{1g}^1, A_{2g}^1, and E_g^2. If one measures scattered light with a polarization in the y direction, only Eg^2 will appear in the Raman spectrum.[18] This can be understood by considering the nature of the atomic displacements associated with the phonon modes. If a phonon mode A_{1g} is excited, the tensor implies that the polarization induced by the incident electric field $\xi_0 = (\xi_{x0}, \xi_{y0}, 0)$ has the same direction as ξ_0. So the A_{1g}-type phonon has $d\chi_{xy}/dQ = 0$. On the other hand, a
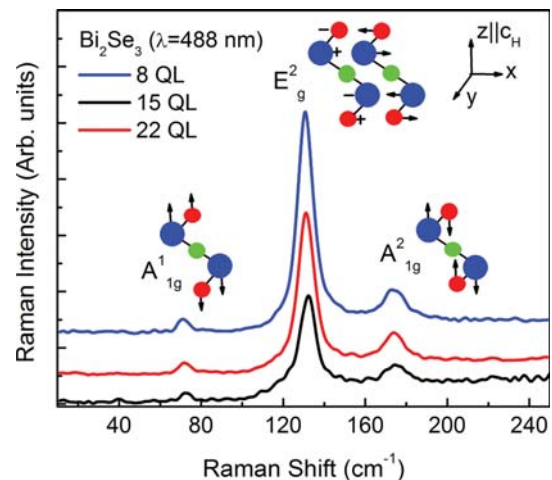

FIG. 3. (Color online) Calibrated intensity ratio of out-of-plane mode (A_{1g}^2) to that of in-plane mode (E_g^2). The inset is the schematic of vibrational modes.

FIG. 4. (Color online) Raman spectra of Bi_2Se_3 FQLs in the 10–250 cm^{-1} region. Three spectra are taken at different thicknesses of the sample. The displacement patterns of E_g^2, A_{1g}^1, and A_{1g}^2 phonon modes are shown in inset. The light is incident along z and polarized along x directions.

TABLE II. Raman peaks in FQLs Bi_2Se_3 film.

Thickness	A^1_{1g}	E^2_g	A^2_{1g}	Comment
$\sim 8\,nm$	70.6	131	173.4	Our work
$\sim 15\,nm$	72.4	132	174.7	
$\sim 22\,nm$	71.5	131.2	174.2	
Bulk	72	131.5	174.5	Ref. 18
Calculated	67.5	121	157.5	

TABLE III. Raman peaks in FQLs Sb_2Te_3 film.

	E^1_g	A^1_{1g}	E^2_g	A^2_{1g}	Comment
Sub-40 nm	35.1	69.8	114.5	167.5	Our work
Calculated	46	62	113	166	Ref. 22

$\sim 114\,cm^{-1}$ corresponds to Eg^2 (TO), and $\sim 165\,cm^{-1}$ corresponds to A^2_{1g} (LO). The agreement with the calculative data is good.

B. Resonant Raman scattering

Raman spectroscopy can provide additional information if the resonant Raman scattering (RRS) occurs. When the excitation line is tuned into an electronic absorption band, some of the Raman bands, which are related to the electronic transition that is responsible for the absorption, will be greatly enhanced. This means that the equilibrium conformation of the molecule is distorted along the normal coordinate of the given Raman line in the transition from the ground to the excited electronic state. Theoretically, a change in the polarizability $(\alpha_{p\sigma})_{mn}$ due to the electronic transition $(m \rightarrow e \rightarrow n)$ can be written as[31]

$$(\alpha_{p\sigma})_{mn} = \frac{1}{h}\sum \left(\frac{M_{me}M_{en}}{\upsilon_{em} - \upsilon_0 + i\Gamma_e} + \frac{M_{me}M_{en}}{\upsilon_{en} + \upsilon_0 + i\Gamma_e} \right), \quad (2)$$

where m, n, and e are the electronic states, υ_{en} and υ_{em} are the frequencies corresponding to the energy differences between the states and incident laser beam frequency υ_0. As υ_0 approaches υ_{em}, the denominator of the first term in the brackets of Eq. (2) becomes very small. Hence, this term—the resonance term—becomes so large that the intensity of the Raman band at $\upsilon_0 - \upsilon_{mn}$ increases strongly. This selectivity is important not only for identifying vibrations of this particular energy in a complex spectrum, but also for locating its electronic transitions in an absorption spectrum. Therefore, RRS has a wide range of application, including determination of the electronic states.

The obtained Raman scattering spectra of FQL Bi_2Te_3 and Bi_2Se_3 taken at 633 nm wavelength are shown in Fig. 6. Non-resonant Raman spectra taken at 488 nm is also shown for comparison. The same polarization setup (i.e., $z(xx)\bar{z}$) and the same conditions (i.e., accumulation time, laser power, and objective) were maintained for both 488 nm and 633 nm laser excitation. The strong resonance was observed as the excitation laser energy (1.96 eV) creates a vibrational state near the electronic state of the band structure. This is exactly what is expected for both Bi_2Se_3 and Bi_2Te_3, since, at Γ point, there exists a conduction band (electronic excited state), which lies at 633 nm ($\sim$1.96 eV) above the valence band maximum (ground state).[34]

Another intriguing observation from Fig. 6 is that, at 488 nm (2.54 eV) the off-resonance excitations, the E_g (TO) mode is the dominant feature in the spectra, while, at the resonance with a laser excitation at 633 nm (1.96 eV), the A_{1g} (LO) becomes the dominant mode. For Bi_2Te_3, a strong evolution of the A^2_{1g} mode (LO) is observed in Fig. 6 and no Eg^2 mode (TO) can be observed under the resonant condition,

phonon of the type E_g possesses displacements in both the x and y directions, i.e., in plane vibration. An incident electric field, ξ_{x0}, thus induces polarization changes in both directions, and the scattered light contains polarization components in both these directions, i.e., $d\chi_{xx}/dQ \neq 0$, $d\chi_{xy}/dQ \neq 0$.

For Bi_2Se_3 crystal, the Raman bands appear in the higher frequency range than that of Bi_2Te_3. This is due to the stronger bonding forces compared to Bi_2Te_3 and Sb_2Te_3. This fact is also supported by the small atomic distances in Bi_2Se_3.[18] In addition, the Se atom is lighter than Te atom, so that, when laser light interacts with the material, the Se atoms vibrate stronger, producing Raman bands with higher intensity. Another important observation is that there is no IR mode in the spectra of FQLs Bi_2Se_3 films as compared to that of Bi_2Te_3 films. According to Ref. 18, in Bi_2Te_3 crystals, both $E\perp C$ and $E\|C$ polarizations are allowed to interact. However, in Bi_2Se_3, only $E\perp C$ polarization (E_u mode) on the cleavage planes is possible. As a result, the E_u mode, which is in-plane vibration, does not reveal itself, even when the thickness of exfoliated Bi_2Se_3 goes down to a few quintuple layers along the C_H axis.

Let us discuss now the non-resonant Raman spectrum of antimony telluride, which is shown in Fig. 5. The calculated frequencies of the Raman active phonon modes for Sb_2Te_3 crystal were reported in Ref. 22. For convenience, we listed them in Table III. The calculations were preformed within the framework of density functional perturbation theory.[22] Comparing our results with the calculated values, we can conclude that, in Sb_2Te_3 FQL, the peak at $\sim 35\,cm^{-1}$ corresponds to E_g^1 (TO), $\sim 70\,cm^{-1}$ corresponds to A_{1g}^1 (LO),

FIG. 5. (Color online) Raman spectra of sub-40 nm Sb_2Te_3 at 488 nm laser excitation.
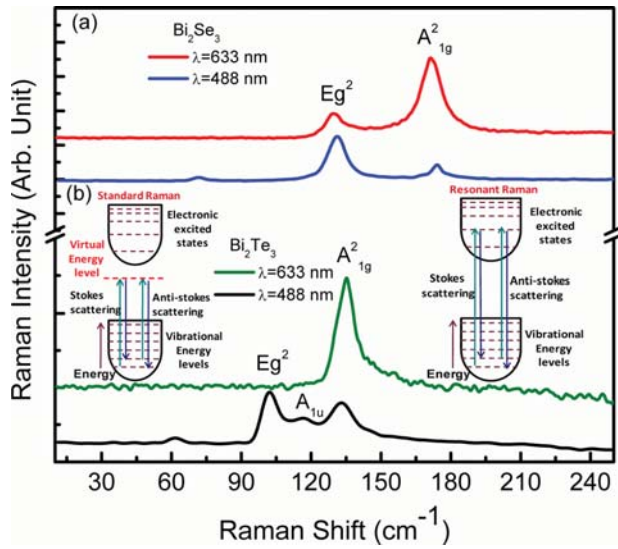
FIG. 6. (Color online) Resonant Raman spectra acquired at 633 nm (1.96 eV) excitation and non-resonant Raman spectra acquired at 488 nm (2.54 eV) excitation: (a) Bi_2Se_3; (b) Bi_2Te_3.

i.e., 633 nm laser light. Similarly, in the case of Bi_2Se_3, the intensity of A_{1g}^2 mode becomes larger than that of Eg^2 mode. This evolution is analogous to the one observed by some of us in ZnO nanocrystals,[35,36] where, at the resonant conditions, the LO is dominant and no TO phonons are observed. The dominance of LO modes can be explained by an analysis of how these phonons couple to the electronic systems. The LO phonon-electron interaction is mediated via Frohlich interaction,[37] and the intensity of the LO modes might be strongly enhanced. On the other hand, the Frohlich coupling cancels for E_g phonons. The properties of the longitudinal optical modes are of great interest, because of the fact that their long range electrostatic field can couple and interact with electrons. This LO phonon-electron interaction can diminish the performance of optoelectronics devices[38] or, on the other hand, can be utilized in phonon engineering to create devices such as cascade lasers.[39]

C. Substrate effects

In order to extend the use of Raman spectroscopy as the nanometrology tool for thin films, one needs to study how the Raman signatures of thin films are affected when they are placed on different substrates other than the regular SiO_2/Si. Previously, we reported that the Raman phonon peaks undergo modification when graphene is placed on other substrates due to changes in the nature and density of the defects, surface charges, and different strength of the graphene–substrate bonding.[40] After taking Raman spectra

TABLE IV. Raman peaks in FQLs Bi_2Se_3 film on different substrate.

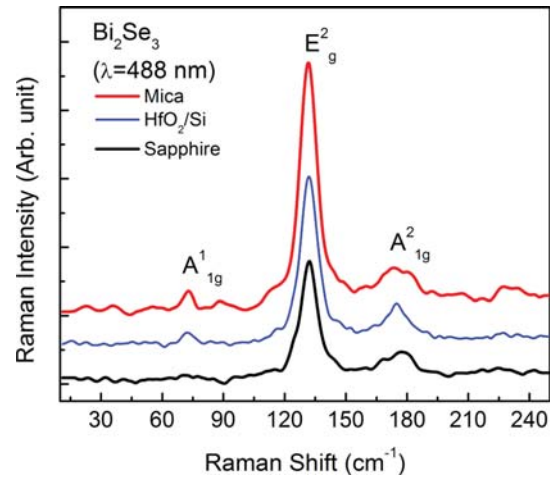| Substrate	A_{1g}	E_g	A_{1g}
SiO_2/Si	71.5	131.2	173.6
Mica	72.9	131.4	174.5
HfO_2/Si	71.9	131.7	175.0
Sapphire	…	133.3	177.1

FIG. 7. (Color online) Raman spectra of Bi_2Se_3 FQLs on different substrates.

from FQL on the standard SiO_2/Si substrate, we investigated Bi_2Se_3 placed on HfO_2/Si, sapphire, and mica substrates (see Table IV). Figure 7 compares Bi_2Se_3 on different substrate (HfO_2/Si, mica, and sapphire) at 488 nm laser excitation. For sapphire at 488 nm light, the A_{1g}^2 mode shows a blueshift of $4 cm^{-1}$. This could be due to the compressive strain. One can also see that, at 488 nm, the A_{1g}^2 mode splits. Previous Raman studies of our group of graphene layers on glass also indicated that, in some instances, the G peak was split into doublets.[40,41] Random defects or charges on the film-substrate interface can explain the doublets. It is also worthwhile to mention that the adherence of FQL to different substrates was similar. This conclusion could be important for further investigation of topological insulators on different substrates.

V. CONCLUSIONS

We presented results of the detail Raman studies of the few-quintuple-thick films of Bi_2Te_3, Bi_2Se_3, and Sb_2Te_3. The films were prepared by the "graphene-like" mechanical exfoliation from the bulk crystals. It was found that, in some materials, the crystal symmetry breaking in few-quintuple films results in appearance of A_{1u}-symmetry Raman peaks, which are not active in the bulk crystals. Our experimental observation is in agreement with the recent computational studies. The scattering spectra measured under the 633 nm wavelength excitation reveals a number of resonant features, which can also be used for analysis of the electronic and phonon processes in these materials. The obtained results help to understand the physical mechanisms of Raman scattering in the few-quintuple-thick films and can be used for nanometrology of topological insulator films on various substrates.

ACKNOWLEDGMENTS

[1]B. A. Bernevig, T. L. Hughes, and S. C. Zhang, Science **314**, 1757 (2006).

[2]M. Konig, S. Wiedmann, C. Brune, A. Roth, H. Buhmann, L. Molenkamp, X. L. Qi, and S. C. Zhang, Science **318**, 766 (2007).

[3]L. Fu and C. L. Kane, Phys. Rev. B **76**, 045302 (2007).

[4]D. Hsieh, D. Qian, L. Wray, Y. Xia, Y. S. Hor, R. J. Cava, and M. Z. Hasan, Nature **452**, 970 (2008).

[5]H. Zhang, C. Liu, X. Qi, X. Dai, Z. Fang, and S. Zhang, Nature Phys. **5**, 438 (2009).

[6]Y. Xia, D. Qian, D. Hsieh, L. Wray, A. Pal, H. Lin, A. Bansil, D. Grauer, Y. S. Hor, and R. J. Cava, Nature Phys. **5**, 398 (2009).

[7]A. Akhmerov, J. Nilsson, and C. Beenakker, Phys. Rev. Lett. **102**, 216404 (2009).

[8]J. E. Moore, Nature **464**, 194 (2010).

[9]A. F. Ioffe, *Semiconductor Thermoelements* (Nauka, Moscow, 1956); A. F. Ioffe, *Semiconductor Thermoelectric and Thermoelectric Cooling* (Infosearch, London, 1957).

[10]H. J. Goldsmid and R. W. Douglas, Br. J. Appl. Phys. **5**, 458 (1954).

[11]D. A. Wright, Nature **181**, 834 (1958).

[12]G. J. Snyder and E. S. Tobere, Nature Mater. **7**, 105 (2008).

[13]O. B. Yehuda, R. Shuker, Y. Gelbstein, Z. Dashevsky, and M. P. Dariel, J. Appl. Phys. **101**, 113707 (2007).

[14]S. K. Mishra, S. Satpathy, and O. Jepsen, J. Phys.: Condens. Matter **9**(2), 461 (1997).

[15]A. Boyer and E. Cissé Mater. Sci. Eng. B **13**, (1992); M. Wuttig and M. Yamada, Nature Mater. **6**, 824 (2007).

[16]J. O. Jenkins, J. A. Rayne, and R. W. Ure, Phys. Rev. B **5**, 3171 (1972).

[17]W. Kullmann, J. Geurts, W. Richter, N. Lehner, H. Rauh, U. Steigenberger, G. Eichhorn, and R. Geick, Phys. Status Solidi B **125**, 131 (1984).

[18]W. Richter, H. Kohler, and C. R. Becker, Phys. Status Solidi B **84**, 619 (1977).

[19]V. Wagner, G. Dolling, B. M. Powell, and G. Landwehr, Phys. Status Solidi B **85**, 311 (1978).

[20]V. Russo, A. Bailini, M. Zamboni, M. Passoni, C. Conti, C. S. Casari, A. Li Bassi, and C. E. Bottani, J. Raman Spectrosc. **39**, 205 (2008).

[21]L. M. Goncalves, C. Couto, P. Alpuim, A. G. Rolo, F. Völklein, and J. H. Correia, Thin Solid Films **518**, 2816 (2010).

[22]G. C. Sosso, S. Caravati, and M. Bernasconi, J. Phys.: Condens. Matter **21**, 095410 (2009).

[23]A. C. Ferrari, J. C. Meyer, V. Scardaci, C. Casiraghi, F. Mauri, S. Piscanec, D. Jiang, K. S. Novoselov, S. Roth, and A. K. Geim, Phys. Rev. Lett. **97**, 187401 (2006).

[24]I. Calizo, A. A. Balandin, W. Bao, F. Miao, and C. N. Lau, Nano Lett. **7**, 2645 (2007); I. Calizo, F. Miao, W. Bao, C. N. Lau, and A. A. Balandin, Appl. Phys. Lett. **91**, 071913 (2007); I. Calizo, W. Bao, F. Miao, C. N. Lau, and A. A. Balandin, Appl. Phys. Lett. **91**, 201904 (2007); I. Calizo, I. Bejenari, M. Rahman, G. Liu, and A. A. Balandin, J. Appl. Phys. **106**, 043509 (2009).

[25]A. A. Balandin, S. Ghosh, W. Bao, I. Calizo, D. Teweldebrhan, F. Miao, and C. N. Lau, Nano Lett. **8**, 902 (2008); S. Ghosh, D. L. Nika, E. P. Pokatilov, and A. A. Balandin, New J. Phys. **11**, 095012 (2009); A. A. Balandin, Nature Mater. **10**, 569 (2011).

[26]D. Teweldebrhan, V. Goyal, and A. A. Balandin, Nano Lett. **10**, 1209 (2010); D. Teweldebrhan, V. Goyal, M. Rahman, and A. A. Balandin, Appl. Phys. Lett. **96**, 053107 (2010).

[27]M. Z. Hossain, S. L. Rumyantsev, D. Teweldebrhan, K. M. F. Shahil, M. Shur, and A. A. Balandin, Phys. Status Solidi A **208**(1), 144 (2011); M. Z. Hossain, S. L. Rumyantsev, K. M. F. Shahil, D. Teweldebrhan, M. Shur, and A. A. Balandin, ACS Nano **5**(4), 2657 (2011).

[28]A. Casian, I. Sur, H. Scherrer, and Z. Dashevsky, Phys. Rev. B **61**, 15965 (2000).

[29]K. S. Novoselov, A. K. Geim, S. V. Morozov, D. Jiang, Y. Zhang, S. V. Dubonos, I. V. Grigorieva, and A. A. Firsov, Science **306**, 666 (2004).

[30]K. M. F. Shahil, M. Z. Hossain, D. Teweldebrhan, and A. A. Balandin, Appl. Phys. Lett. **96**, 153103 (2010).

[31]P. Y. Yu and M. Cardona, *Fundamentals of Semiconductors-Physics and Materials Properties*, 3rd ed. (Springer, Heidelberg, 2005).

[32]W. Cheng and S. F. Ren, Phys. Rev. B **83**, 094301 (2011).

[33]Y. Zhang, K. He, C. Z. Chang, C. L. Song, L. L. Wang, X. Chen, J. F. Jia, Z. Fang, X. Dai, W. Y. Shan, S. Q. Shen, Q. Niu, X. L.Qi, S. C. Zhang, X. C. Ma and Q. K. Xue, Nature Phys. **6**, 584 (2010).

[34]S. K. Mishra, S. Satpathy, and O. Jepsen, J. Phys.: Condens. Matter **9**, 461 (1997).

[35]K. Alim, V. A. Fonoberov, and A. A. Balandin, Appl. Phys. Lett. **86**, 053103 (2005).

[36]K. A. Alim, V. A. Fonoberov, M. Shamsa, and A. A. Balandin, J. Appl. Phys. **97**, 124313 (2005).

[37]A. K. Sood, J. Menendez, M. Cardona, and K. Ploog, Phys. Rev. Lett. **54**, 2111 (1985).

[38]A. A. Kiselev, K. W. Kim, and M. A. Stroscio, Phys. Rev. B **59**, 10212 (1999).

[39]V. P. Elestin and Y. V. Kopaev, Solid State Commun. **96**, 897 (1995).

[40]I. Calizo, S. Ghosha, W. Bao, F. Miao, C. N. Lau, and A. A. Balandin, Solid State Commun. **149**, 1132 (2009).

[41]I. Calizo, W. Bao, F. Miao, C. N. Lau, and A. A. Balandin, Appl. Phys. Lett. **91**, 201904 (2007).